

GMaKE: Galaxy Morphology and Kinematics Estimator

RUI XUE¹ AND HAI FU¹

¹Department of Physics & Astronomy, University of Iowa, 203 Van Allen Hall, Iowa City, IA 52242, USA

ABSTRACT

GMaKE is a toolkit for evaluating galaxy morphology and kinematics from astronomical 2D images or 3D spectral cubes. It takes the advantages of various existing programs for galaxy modeling and essentially serve as a flexible wrapper for quantifying the galaxy geometry and kinematics structures through parameterized models, with varieties of parameter fitting and error estimation algorithm to choose from. With a flexible modulated code design, the toolkit can easily incorporate an arbitrary galaxy emission models with a proper adapter and perform parameter optimization to search for most proper model solutions.

With the modern interferometer dataset in mind, the model-data comparison can be performed in either spatial or visibility domain, which avoid the no-linear effect in image deconvolution.

Because we construct synthetical radio/optical spectral or continuum images at different wavelengths/frequencies using realistic instrumental response functions from a galaxy model characterized by shared physical geometry and independent line/continuum emissivity functions, the code is capable to fit all available data with a unified model, even under the complicated situation in which the data are contributed by multiple blending objects and absorptions/emission lines.

Keywords: galaxies: formation — galaxies: structure — galaxies: kinematics — methods: data analysis

Contents			
1. Introduction	1	A. ALMA archival data of BX610	6
2. Modeling Overview	2	B. SINFONI observations of BX610	6
2.1. Spectral Line Emission	2	C. Example of Input Files	6
2.1.1. Geometry and Emissivity Model	2	D. Comparison Summary	6
2.1.2. Kinematic and Dynamical Model	3	E. keywords	6
2.1.3. Emission Model in the $(\alpha, \delta, v/\nu/\lambda)$ domain	3	F. Diagnostic Plots	6
2.2. Simulated Observations	3	G. Dynamical Mass Calculation	8
2.2.1. Visibility	3		
2.2.2. Spectral-Cube/Image	4		
2.3. Model Fitting Algorithms	4		
3. Examples	5	1. INTRODUCTION	
3.1. ALMA Line/Continuum observation of High-redshift galaxies	5	A fundamental aspect of the galaxy evolution study is to understand their dynamical structure and matter distributions. The majority of such information comes from their electromagnetic radiation: the emission and absorption at different wavelength can trace various matter components at certain physical conditions, along the line of sight; while spectral line features can further reveal the galaxy kinematics through the Doppler shift. Therefore, the kinematic and morphological analyses based on spectroscopy or imaging are the essential technique for galaxy study.	
3.2. IFU observations of High-redshift Galaxies	5	While many specialized tools have been developed for such measurement in last decades to overcome the limitations of resolution and sensitivity inherent in the	
4. Discussions	5		
4.1. Image vs. UV domain analysis for Interferometric data	5		
4.2. Performance	5		
4.2.1. Object/Line Decomposition	5		
4.2.2. Source Extraction	5		
5. Summary	5		

observed data, we have identified two major limitations in existing development: 1) many programs are focused on the application based on a single data set or type; 2) most codes are exclusively designed for either continuum or spectral line emission (even restricted to a single object or one line component). The former design limits the joint constrain power from multi-wavelength datasets in different forms (e.g., images, slit-spectroscopy, etc.), which become widely available in the modern astronomy "big-data" era. The latter coding principle unnecessarily requires the original dataset to be decomposed before any analysis. As object/line blending and coexisting of line and continuum emission are common in astronomical data, this additional layer of data manipulation introduce uncertain especially in low SNR conditions.

GMaKE

footnote^{https://github.com/r-xue/GMaKE} is a Python-based modeling code for evaluating galaxy morphology and kinematics from multiple-band astronomical observations. GMaKE first builds an intrinsic galaxy line and/or continuum emission model based on the parameterized spatial and kinematical models of different components, and then pass the result to simulated observations to generate mockup data, which can be directly compared with observational datasets. Different from previous fitting algorithms which were usually applied to 2-dimension single dataset, our fitting method can be simultaneously applied to multiple datasets obtained in different forms (e.g., images, spectral-cubes, or interferometric visibilities). The forward-modeling approach can not only provide a joint constraint from all available observational evidence at different spatial/spectral resolutions, but also simplify the model uncertainty estimation by minimizing advanced data manipulations (e.g., continuum subtraction for diffuse line emission, interferometry imaging/CLEAN of low-SNR data without zero-spacing information).

While this is not the first program fitting spectral cube, the code is designed to offer some uniq advantages:

- Different Model Fitting Methods, emcee, amoeba
- Visibility DataSet
- Friendly parameter format
- Physical Models

The paper is organized as follows. We present the philosophical principle of our code design and technical details in Section 2. It is followed with multiple application examples from Section 3: a rich multi-wavelength datasets of normal star-forming high-redshift galaxy, including both ALMA radio and IFU IR data; a synthetic moderately resolved galaxy based on high-resolution nearby galaxy dataset; a high-z galaxy with

rest-frame Ly α and UV imaging. Section 4 compares the algorithm with previous modeling methods. Finally, we summarize the future perspective of expanding capability and application of GMaKE.

2. MODELING OVERVIEW

In this section, we give a quick overview of GMaKE workflow.

One important design choice in GMaKE is that we built emission model on the physical dimension and then transform the emission into the native data form obtained in observations. Therefore, the application will require that the data were provide along with correct WCS system or observational metadata (e.g., u-v sampling in interferometric data)

We recap some feature but emphasize what we improved.

2.1. Spectral Line Emission

To model spatially resolved spectral line emission of galaxies, we require a parameterized prescription for the line emissivity and galaxy kinematic structures. We start with a first-order base model by assuming the line emission arises from an axial-symmetry disk morphology with organized rotation. The second-order morphology alternation or other motion components can be added upon it. In this section, we describe the geometry and kinematics setup in our models, with second-order features described at the end.

2.1.1. Geometry and Emissivity Model

We set up a 3D Cartesian coordinate system with the presumed galactic disk on the (x, y) plane. The emissivity distribution is parameterized as $I(r, z)$, which depends on the galactocentric distance $r = \sqrt{x^2 + y^2}$ and the above-plane height z . The default option is,

$$I(r, z) = I(r)I(z) \quad (1)$$

$$\propto \exp \left\{ -b_n \left[\left(\frac{r}{r_e} \right)^{1/n} - 1 \right] \right\} \exp \left(-\frac{z^2}{2h_z^2} \right) \quad (2)$$

This presents a Sérsic (1963) surface brightness (SB) radial profile with a half-light radius of r_e and a Sérsic index of n . In addition, it assumes a Gaussian brightness distribution perpendicular to the galactic plane with a characteristic disk thickness of h_z . The b_n value in the radial profile component will depend on the Sérsic index. A Gaussian profile, an exponential profile (Freeman 1970), or the classic de Vaucouleurs (1948) profile, can be obtained by fixing the Sérsic index $n = 0.5, 1$, or 4 , with the corresponding b_n value of $0.686, 1.678$, and 7.669 , respectively.

Our program also allows users to adopt arbitrary radial or vertical profile analytical forms through an algebraic expression in parameters files (see Section 2.3 and Table 3 for more details). In addition, some common

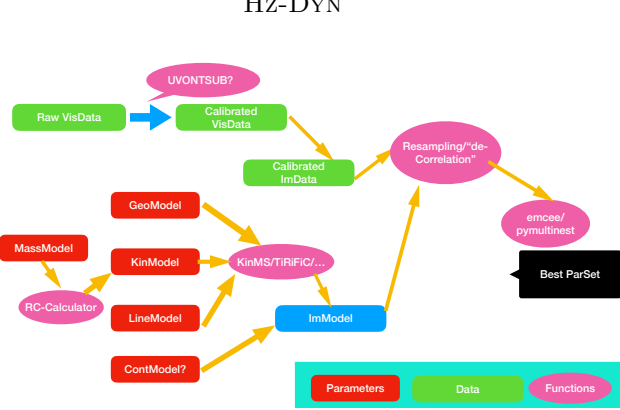


Figure 1. code structure/workflow: xy-version/uv-version

analytical radial/vertical profile functions are written as built-in options, such as the $\text{sech}^2(z/2h_z)$ “isothermal” vertical distribution (van der Kruit & Searle 1981) or a more general form from van der Kruit (1988),

$$I(z) \propto \text{sech}^{2/n} \left(\frac{nz}{2h_z} \right). \quad (3)$$

2.1.2. Kinematic and Dynamical Model

The model kinematical structure is also specified in the same Cartesian coordinate system. The default option is described by a well-organized rotation with a rotational velocity depending on the galactocentric distance. The rotation curve can be specified as a tabulated radial profile, an analytical function form.

We also provide an option of using a rotation curve derived from a dynamical model, which is based on the gravitational potential of specified disk/halo-like mass distributions (see Table 3). In this option, the parameter set describing mass distributions is translated into a gravitational potential model using the PYTHON module `galpy` (Bovy 2015), which also calculates the rotational velocity expected on the galactic plane. The mass distribution can be described by mass components mimicking the common galactic disk or DM halo distribution, or directly scaled from the disk-plane light distribution using a constant light-to-mass ratio.

The velocity dispersion is assumed to be uniform in the galaxy by default, although a radial or vertical dependency can be added. The potential-based dynamical model does not account of the dispersion-based support to the disk, therefore it’s only strictly correct if the ratio of bulk rotation velocity v_{rot} to the turbulent motion σ_v is significantly larger than unity (i.e., rotation-dominated rather than pressure-supported), which may be not rule for high- z disks and current observations become unable to differentiate between pressure-supported and rotation-dominated galaxies (see, e.g., Tamburro et al. 2009 and Stilp et al. 2013).

2.1.3. Emission Model in the $(\alpha, \delta, v/\nu/\lambda)$ domain

We follow the Monte Carlo approach to produce a spectral cube model. The procedure essentially gener-

ates a set of “cloudlets”, with their spatial positions and velocity vectors randomly assigned following the specified galaxy morphology and kinematics structure distribution. After a spatial-to-sky coordination transform, and they are integrated into a position-position-velocity (PPV) space using their on-sky position and the line-of-sight velocity components. The same “tilted-ring” principal (Rogstad et al. 1974) is adopted for other similar modeling codes such as `GIPSY/GALMOD`, `3DBarolo`, or `TiRiFiC` (van der Hulst et al. 1992; Józsa et al. 2007; Di Teodoro & Fraternali 2015; Bouché et al. 2015)

The coordinate transformation in our program requires the geometry setup of the (x,y) plane relative to the sky plane (α, δ) , which include the (x, y) plane origin in WCS coordinates, the inclination of the “ring” and position angle of the major axis of its on-sky projection. The line-of-sight radial velocity can be further transformed into the wavelength of frequency of spectral lines when the galaxy systematic velocity (or its redshift) and rest-wavelength/frequency are provided.

We design the program to model multiple emission components and objects. At the same time, all emission components are integrated and mapped into different datasets through simulated observation described below.

2.2. Simulated Observations

One critical design goal of `GMaKE` is the implementation of forward modeling approach: The models will be mapped into the observational datasets for parameter fitting through simulated observations. Depending on the types of observation and the data format, the simulation will require different metadata and call different subroutines components. We describe the mapping process details for three supported types of data in this section.

2.2.1. Visibility

The program is able to directly read the radio interferometric visibility data stored in the CASA Measurement

Set (MS) format¹ using the `python-casacore`² module. `python-casacore` provides a PYTHON interface to the `casacore` library, which is standalone from the CASA package. It allows direct access and manipulation of the essential information stored in MS tables, including the complex visibility data, u - v coordinates, and weights. We convolve the intrinsic spectral cube or image model with the telescope primary beam, and then transfer the results into a visibility model with the u - v coordinates from MS tables, using `galario` (Tazzari et al. 2018). The visibility model is then exported to the MS model column for evaluation or imaging. While the current implementation only supports MS, the program should also work if a proper data conversion is done.

2.2.2. Spectral-Cube/Image

When the data is provided as images or spectral-cubes in the FITS format, the program will convolve the intrinsic model with the instrument response functions (specifically, the point-spreading function, PSF and spectral line-spreading function, LSF). These functions can be specified in analytical forms (e.g., Gaussian / Moffat), or a noiseless kernel. To perform the coordinate transform, the program will use the World Coordinate System (WCS) information stored in data files, which are presumed to follow the standard FITS header convention (Greisen & Calabretta 2002). The spatial 2D and spectral 1D convolution is performed using a selection of FFT libraries available on different computing platforms (e.g., `py-fftw`, `scipy-fftw`, or `Intel MKL-FFT`)

2.3. Model Fitting Algorithms

For spectral cube data, we perform model fitting of three-dimensional structure rather than just two-dimensional velocity field, which is limited by beam smearing and extraction methods.

We offer a flexible choice of free parameters in model fitting in `GMaKE`. In addition, we implement a mechanism in the parameter file syntax, which can tie the mathematical relationships among fitting parameters and specify analytical function forms for some model attributes through simple algebraic expressions. The first capability can be used to specify inherent relations among model parameters (e.g., a constant ratio among line brightness) and the latter will provide users with the flexibility of experimenting different model assumptions (e.g. rotational curves or surface brightness radial/vertical profiles, see Table 3).

While there is no limitation on the number of free parameters, increasing parameter dimensions and complicity of the corresponding likelihood function will still rapidly lead to common difficulties faced by all mini-

mization/optimization methods used in any model fitting programs, e.g., dependency of initial parameter guesses, local versus global minima, parameter degeneracy, error estimations, etc. Additional complications came from the error characterization for low-S/N data with correlated noise among data points. As a practical solution, we decide to implement multiple fitting algorithms under the program.

The fitting algorithm options in our program fall into four catalogues: Nelder-Mead (a.k.a. downhill simplex or amoeba), Levenberg-Marquardt (LM), grid searching (a.k.a. brute-force), and the Markov Chain Monte Carlo (MCMC), variants of which are directly built in our code or implemented as optional PYTHON module dependence, including `emcee`³ (Foreman-Mackey et al. 2013) and `lmfit` (Newville et al. 2016). We note that the wide range of fitting options is not intended to benchmark different algorithms, which may be based on different statistical assumption/criteria and come with different computational cost. For example, the Nelder-Mead method can provide a fast and simple solution in a high-dimension parameter space by minimizing a scalar value (usually χ^2 , see below). However, it does not provide a direct assessment of model uncertainty. On the other hand, a Bayesian MCMC can provide a robust assessment of model parameter confidence levels directly from the posterior distribution sampling, but is computationally intensive and may require good initial parameter guesses. The implementation of various fitting algorithms is to provide them under the same user interface, which generates similar-formatted diagnostic plots and log files for inspections on the optimization process. In addition, the log files can be re-used for next fitting exercise, with the initial guess filled with best-fit parameter result from the last run. All of these features are designed to provide users a flexible model fitting program, which can adopt the suitable algorithms for different situations. This will be ideal for fitting experiments and help analyses.

$$\ln p = -\frac{1}{2} \sum_i \left[\frac{(I_i - M_i)^2}{s_i^2} + \ln(2\pi s_i^2) \right]. \quad (4)$$

or the χ^2 value,

$$\chi^2 = \sum_i \left[\frac{(I_i - M_i)^2}{s_i^2} \right]. \quad (5)$$

Here, I_i , M , and s present the data, model, and uncertainty values of the i -th voxel/pixel in the datasets. For visibility data, a vector subtraction is used. For a scalar-based algorithm like the Nelder-Mead method, the best-fit parameters is likely unaffected by this as-

¹ <https://casa.nrao.edu/Memos/229.html>; van Diepen (2015)

² <http://casacore.github.io/python-casacore/>

³ <http://dfm.io/emcee>

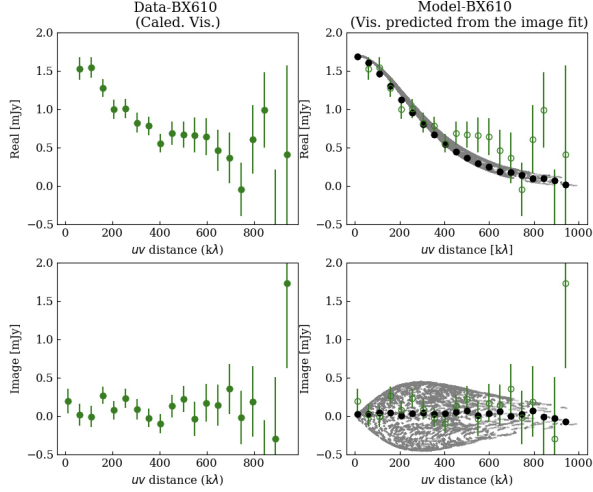


Figure 2. Highlight the advantage of searching for high spatial frequency information in UV.

sumption, However, the erro estmation from other meth-
ods (like MCMC and LM) will likely be underestimated
as the noise covraiance among adjacent data ppoints
areignored.

The prescription assume an apprximnation that all
data points are indepdenden with a Gaussian noise char-
acterized by s_i . For an oversampled data image, the
noise correlation among differnet pixels are rather cor-
rellated. Therefore we provide an option to samplethe-
hexgaon grid spacing by approxminate half PSF size,
and only use the While this doesn't

3. EXAMPLES

3.1. ALMA Line/Continuum observation of High-redshift galaxies

Results.

Image vs. UV.

3.2. IFU observations of High-redshift Galaxies

Use the HST image as prior

Tacchella et al. (2018)

BX610: CO7-6 and CI2-1

4. DISSCUSSIONS

This is a expandable framwork but a program

4.1. Image vs. UV domain analysis for Interferometric data

- no CLEAN

- no pixel gridding

deproject nearby galaxies to distant galaxies.

4.2. Performance

4.2.1. Object/Line Decomposition

4.2.2. Source Extraction

5. SUMMARY

Table 1. ALMA Observations of BX610

Project Code	P.I.	Band	Resolution	LAS	Lines	Δv	Cont.Freq.	ToS
2013.1.00059.S	Aravena, M.	4	0''.31	1''.63	$\text{CO } J = 4 \rightarrow 3 / [\text{C I}]^3 P_1 \rightarrow ^3 P_0$	15.0 km s ⁻¹	140GHz	1.5 hr
2015.1.00250.S	Aravena, M.	6	0''.25	1''.37	$\text{CO } J = 7 \rightarrow 6 / [\text{C I}]^3 P_2 \rightarrow ^3 P_1$	18.5 km s ⁻¹	233GHz	1.1 hr
2017.1.01045.S	Brisbin, D.	4	0''.04	0''.57	$\text{CO } J = 4 \rightarrow 3 / [\text{C I}]^3 P_1 \rightarrow ^3 P_0$	3.7 km s ⁻¹	140GHz	3.9 hr

NOTE— ToS: Time-on-Source, the aggregated integration time on the target field; Cont.Freq: the observed continuum frequency; LAS: largest angular scale, the maximal angular size of the spatial structure which the array configuration can observe; Resolution: the synthesized beam size reported in the ALMA archive imaging products.

APPENDIX

A. ALMA ARCHIVAL DATA OF BX610

We obtain the public ALMA data of BX610 from the ALMA Science Archive. Three observations were carried out for the galaxy in 2013, 2015, and 2017 (see Table 1). In all observation, four 1.875-GHz spectral windows were utilized for detecting line and continuum emission. We rerun the ALMA pipeline calibration scripts supplied within the archival products for the raw visibility data using CASA (McMullin et al. 2007). This generated the fully calibrated visibility, and we performed additional manual inspection to flag bad data from a small number of antenna/channel by their abnormal amplitude.

While our program can model data in the *uv* domain, we have imaged the visibility data and model for testing on the image-domain modeling capability as well as quality inspection/visualization. For all imaging, we produce data cubes using the Briggs ROBUST weighting of $R = 0.5$ and the synthesized beams are sampled by at least nine pixels.

In four 1.875-GHz spectral windows, we tuned two of them for detecting continuum emission at 105.1GHz, with the other two centered around 92.2 and 94.0 GHz. The later two windows were targeted to the CO $J = 3 \rightarrow 2$ emission from two different redshifts ($z = 2.67$ and 2.75), which are associated with the SMG and a QSO system previously identified in optical spectra. The channel width of all four spectral windows was set to 7.8125 MHz, which is equivalent to a velocity resolution of $22.5 - 25.5$ km/s.

We calibrated the visibility data using the ALMA pipeline implemented within CASA ver. 5.4.0. We imaged two separate spectral cubes from two line windows, one continuum image from two continuum windows. The imaging pixel was set to $0''.2$, and we adopted an imaging channel width of three times that intrinsic visibility channel, which provides a resolution of ~ 75 km/s for the CO 3-2 line at the expected SMG redshift.

With a robust weighting of $R = 1$, the final imaging achieves a spatial resolution of $\sim 1''.5 \times 1''.2$ in the CO $J = 3 \rightarrow 2$ window. The sensitivity of the continuum image reaches 6.7 uJy/beam, with the line channel sensitivity archive 0.1 mJy/beam. We didn't perform continuum subtraction in the visibility data and instead to choose image-domain subtraction for any identified line emitter on an individual basis.

B. SINFONI OBSERVATIONS OF BX610

C. EXAMPLE OF INPUT FILES

The program will save the results into the a parameter file which contain the best-fit resultsg same parameter file

D. COMPARISON SUMMARY

E. KEYWORDS

F. DIAGNOSTIC PLOTS

Observational data are acquired at most in three dimensions (*x-y-freq/wavelength*). We therefore divided our diagnostic plots into three groups, depending on the number of dimension in which they are presented. Various diagnostic plots can be produced by choosing different dimension combinations and adjusting restribucitions of subregions in which the data are extracted.

1D plots – intensity vs. spectral dimension This is just the display of spectra extracted at various aperture

1D plots – intensity vs. spatial dimension This is the display of radial profile (deprojected) or intensity profile along a spatial slice. or along major minor axis.

1D plots – display of physical properties (for example, radial vs. rotational velocity / dispersion)

2D plots – intensity / velocity centroid / velocity dispersion vs. x-y These two-dimensional representation show the spatial distribution of various physical properties extracted from the data: for example, the integrated

Table 2. Summary

Name	Reference	Type	DataType	Platform/Lang.	Fitting	Availability
2D (velocity-field) Kinematics Fitting						
ROTUR	van Albada et al. (1985)	Tiled-ring	SpectralCube	GIPSY ¹	lmfit	S/B
3D Kinematics Modeling						
GIPSY/GALMOD KinMS	van der Hulst et al. (1992) (Davis et al. 2013)	Tiled-ring Tiled-ring	SpectralCube SpectralCube	lmfit lmfit	GIPSY IDL/Python ²	S/B S/B
3D (spectral-cube) Kinematics Fitting						
TiRiFiC ^{3D} Barolo GalPak ^{3D}	Józsa et al. (2007) Di Teodoro & Fraternali (2015) Bouché et al. (2015)	Tiled-ring Tiled-ring Tiled-ring	SpectralCube SpectralCube SpectralCube	lmfit lmfit lmfit	CASA C++ C++	S/B S/B S/B
2D Morphology Fitting						
GALFIT PHOTUTILS SEXTRACTOR						

NOTE—Modeling and Fitting, not every program provide the fitting function. Many programs also include source detection propuse but this is not one of them,

¹The same algorithm is built-into NEMO/AIPS

²A modified Python-version of KinMS is implemented in GMaKE for generating intrinsic models in the form of spectral cubes

Table 3. Examples of Different Rotational Curve Forms

Type	Description	Keyword
Table	A cubic spline interpolated from a rotation curve table	vrot = [v _{rot,1} , v _{rot,2} , ...] vrad = [r ₁ , r ₂ , ...]
Analytical	an analytical form specified by a math expression a piece-wise RC: v _{rot} linearly increases to v _{max} “arctan”: v(r) = v _{max} $\frac{2}{\pi}$ arctan(r/r _t) “exp”: v(r) = v _{max} [1 - exp(-r/r _t)] “tanh”: v(r) = v _{max} tanh(r/r _t)	vrot = (math_expr, p1, p2, ...) vrot = ('minimum(vrad/p2,1)*p1', v _{flat} , r _t) vrot = ('p1*2/pi*arctan(vrad/p2)', v _{max} , r _t) alt. vrot = ('arctan', v _{max} , r _t) vrot = ('p1*(1-exp(-vrad/p2))', v _{max} , r _t) alt. vrot = ('exp', v _{max} , r _t) vrot = ('p1*tanh(vrad/p2)', v _{max} , r _t) alt. vrot = ('tanh', v _{max} , r _t)
Dynamics	derived from a gravitational potential model	vrot = ('dynamics', model_name)

intensity, spectral line centroid, line widths (typically referred to as moment-0/1/2 images). The first (veolocitiy field) and second (velocity dispersion) moments images

of a spectral cube can help reaveal galaxies kinematic details. However, the a 2D velocity field / dispersion collapsed the 3D PPV structure into is a limited represen-

```
#####
#optimize          # optimization setup
# key/min/max, etc.
#####

vsys@co76      -120.        +280.        100.
# note: we tie vrot[1:4] as a single free parameter here; vrot[0] is fixed to 0 still.
#vrot[1:5]@co76 0.          +800.        300.
vdis[0:5]@co76 0.          +800.        80.

p@co76         -61.-80       -61.+80       80.
inc@co76        5.           85.          45.

xypos[0]@co76  356.539321-./3600. 356.539321+./3600. 0.5/3600
xypos[1]@co76  12.8220179445-./3600. 12.8220179445+./3600. 0.5/3600

intfluxco76    0.1          200.0        10.0
sbser[0]@co76  0.01         1.0          1.0
ge_p@co76     90.0-90.0    90.0+90.0   89.
ge_q@co76     1.0          10.0         5.

#xypos[0]@c121 356.539321-./3600. 356.539321+./3600. 2./3600
#xypos[1]@c121 12.8220179445-./3600. 12.8220179445+./3600. 2./3600

intfluxc121    0.1          200.0        10.0
sbser[0]@c121  0.01         1.0          1.0
#ge_p@c121    90.0-90.0    90.0+90.0   89.
ge_q@c121     1.0          10.0         5.

#xypos[0]@h20  356.539321-./3600. 356.539321+./3600. 2./3600
#xypos[1]@h20  12.8220179445-./3600. 12.8220179445+./3600. 2./3600

intfluxh20     0.1          200.0        10.0
sbser[0]@h20  0.01         1.0          1.0
#ge_p@h20     90.0-90.0    90.0+90.0   89.
ge_q@h20      1.0          10.0         5.

intfluxco43    0.1          200.0        0.1
sbser[0]@co43  0.01         1.0          0.01
ge_q@co43     1.0          10.0         5.

intfluxc110    0.1          200.0        0.1
sbser[0]@c110  0.01         1.0          0.01
ge_q@c110     1.0          10.0         5.

#xypos[0]@cont 356.539321-./3600. 356.539321+./3600. 2./3600
#xypos[1]@cont 12.8220179445-./3600. 12.8220179445+./3600. 2./3600

intfluxcont    0.1e-3       10.e-3       10e-3
sbser[0]@cont  0.01         0.30         1.00
alpha@cont     3            4.5          1.00
pscont         8-60          8+60         50
inc@cont       0            45.          30

disk_sdrc     1e5           1e10         1e9
disk_rsersd   0.4           5             5
halo_mvirrc   0.01         100          10

method         'ameba'
putname_replace[['examples/bx610/alma/band4/bx610_','b4_'], ['examples/bx610/alma/band6/bx610_','b6_']]
putname_exclude['cube128x128_','lter0','mfs128x128_','image']
putdir         'examples/bx610/mocois/xyb46dm128rc_ab'
```

Figure 3. Highlight the advantage of searching for high spatial frequency information in UV.

tation of the intrinsic gas kinematics within a galaxy due to observational effect such as low S/N or beam smearing, and the result may depend on extraction methods.

but all of them are subjected to the extraction methods and observational effect (low S/N, beam smearing). If we restrict the data into a small spectral range, then we can create a channel maps

2D plots – intensity / velocity centroid / velocity dispersion vs. r-freq/wavelength

3D plots – rendering

G. DYNAMICAL MASS CALCULATION

We present the mass and velocity relation in an equilibrium system as,

$$V_0^2 = \sum V_i^2 = \frac{G}{R} \sum \eta_i M_i \quad (G1)$$

or its dimensionless form,

$$\left(\frac{V_0}{\text{km s}^{-1}} \right)^2 = 4.3 \left(\frac{R}{\text{kpc}} \right)^{-1} \sum \eta_i \frac{M_i}{10^6 M_\odot} \quad (G2)$$

Here M is the enclosed mass within R , and η is a coefficient for the gravitational force which only depends on the mass distribution, with a value of unity for a halo-like spherical symmetric distribution. On the other hand, V_0 is a rotational velocity value at R if the system is only rotationally supported.

For a turbulent disk with an exponential radial profile, i.e., $\Sigma(R) \propto \exp(-R/r_s)$, an isothermal vertical profile $\rho(z) \propto \text{sech}^2(z/2h_z)$, and an isotropic velocity dispersion, Burkert et al. (2010) shows a correction is required to calculate V_0 from the observed rotational velocity v_{rot} .

$$V_0^2 = V_{\text{rot}}^2 + 2\sigma^2 \left(\frac{r}{r_d} \right) \quad (G3)$$

$$\eta = \frac{4y^3 [I_0(y)K_0(y) - I_1(y)K_1(y)]}{1 - e^{2y}(1 + 2y)}, \quad (G4)$$

where v_{rot} is the observed rotational velocity, $y \equiv R/(2r_s)$, and I_i and K_i are the modified Bessel functions (see Binney & Tremaine 2008, § 2.6). While Equation ?? is suitable for the scenario where the mass is dominated by a DM halo or a stellar bulge, we adopt Equation ?? because the gravitational potential is likely dominated by a gas-rich disk in our case.

For a spherical isothermal mass distribution ($\rho \propto r^{-2}$) with an isotropic velocity dispersion,

$$\eta M_{\text{dyn}} = \frac{V_0^2 R}{G} = 2.325 \times 10^5 M_\odot \left(\frac{V_0}{\text{km s}^{-1}} \right)^2 \left(\frac{R}{\text{kpc}} \right), \quad (G5)$$

A dynamical mass can be estimated from the ordered rotation and velocity dispersion using the following relation,

$$\eta M_{\text{dyn}} = \frac{V_0^2 R}{G} = 2.325 \times 10^5 M_\odot \left(\frac{V_0}{\text{km s}^{-1}} \right)^2 \left(\frac{R}{\text{kpc}} \right), \quad (G6)$$

where

in which we account the pressure and rotational support into the coefficient.

$$V_0^2 = V_{\text{rot}}^2 + 2\sigma^2 \quad (G7)$$

$$\eta = 1 \quad (G8)$$

where σ is the projected 1D velocity dispersion.

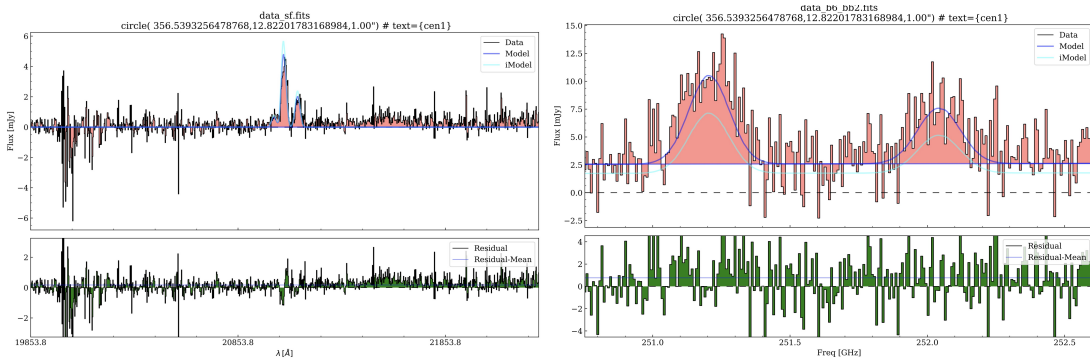


Figure 4. Highlight the advantage of searching for high spatial frequency information in UV.

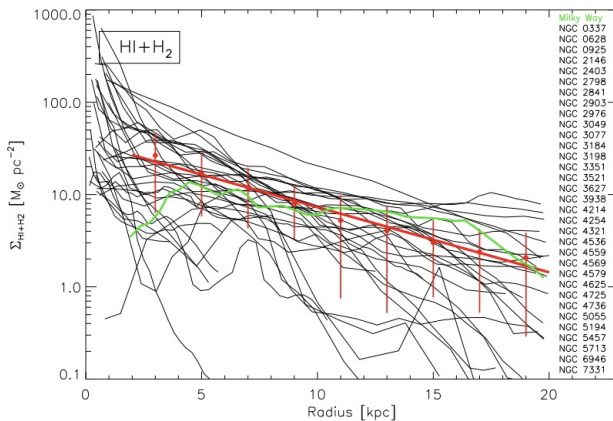


Figure 5. 1D diagnostic plots. Intensity vs. spatial: SB radial profile (after deprojection), Highlight the advantage of searching for high spatial frequency information in UV.

REFERENCES

- Binney, J., & Tremaine, S. 2008, Galactic Dynamics: Second Edition (Princeton University Press).
<http://adsabs.harvard.edu/abs/2008gady.book.....B>
- Bouché, N., Carfantan, H., Schroetter, I., Michel-Dansac, L., & Contini, T. 2015, AJ, 150, 92, doi: [10.1088/0004-6256/150/3/92](https://doi.org/10.1088/0004-6256/150/3/92)
- Bovy, J. 2015, ApJS, 216, 29, doi: [10.1088/0067-0049/216/2/29](https://doi.org/10.1088/0067-0049/216/2/29)
- Burkert, A., Genzel, R., Bouché, N., et al. 2010, ApJ, 725, 2324, doi: [10.1088/0004-637X/725/2/2324](https://doi.org/10.1088/0004-637X/725/2/2324)
- Davis, T. A., Alatalo, K., Bureau, M., et al. 2013, MNRAS, 429, 534, doi: [10.1093/mnras/sts353](https://doi.org/10.1093/mnras/sts353)
- de Vaucouleurs, G. 1948, Annales d'Astrophysique, 11, 247
- Di Teodoro, E. M., & Fraternali, F. 2015, MNRAS, 451, 3021, doi: [10.1093/mnras/stv1213](https://doi.org/10.1093/mnras/stv1213)
- Foreman-Mackey, D., Hogg, D. W., Lang, D., & Goodman, J. 2013, PASP, 125, 306, doi: [10.1086/670067](https://doi.org/10.1086/670067)
- Freeman, K. C. 1970, The Astrophysical Journal, 160, 811, doi: [10.1086/150474](https://doi.org/10.1086/150474)
- Greisen, E. W., & Calabretta, M. R. 2002, A&A, 395, 1061, doi: [10.1051/0004-6361:20021326](https://doi.org/10.1051/0004-6361:20021326)
- Józsa, G. I. G., Kenn, F., Klein, U., & Oosterloo, T. A. 2007, A&A, 468, 731, doi: [10.1051/0004-6361:20066164](https://doi.org/10.1051/0004-6361:20066164)
- McMullin, J. P., Waters, B., Schiebel, D., Young, W., & Golap, K. 2007, Astronomical Data Analysis Software and Systems XVIII, 376, 127
- Newville, M., Stensitzki, T., Allen, D. B., et al. 2016, Lmfit: Non-Linear Least-Square Minimization and Curve-Fitting for Python, Astrophysics Source Code Library. <http://ascl.net/1606.014>
- Rogstad, D. H., Lockhart, I. A., & Wright, M. C. H. 1974, ApJ, 193, 309, doi: [10.1086/153164](https://doi.org/10.1086/153164)
- Sérsic, J. L. 1963, Boletin de la Asociacion Argentina de Astronomia La Plata Argentina, 6, 41
- Tacchella, S., Carollo, C. M., Förster Schreiber, N. M., et al. 2018, ApJ, 859, 56, doi: [10.3847/1538-4357/aabf8b](https://doi.org/10.3847/1538-4357/aabf8b)
- Tazzari, M., Beaujean, F., & Testi, L. 2018, MNRAS, 476, 4527, doi: [10.1093/mnras/sty409](https://doi.org/10.1093/mnras/sty409)

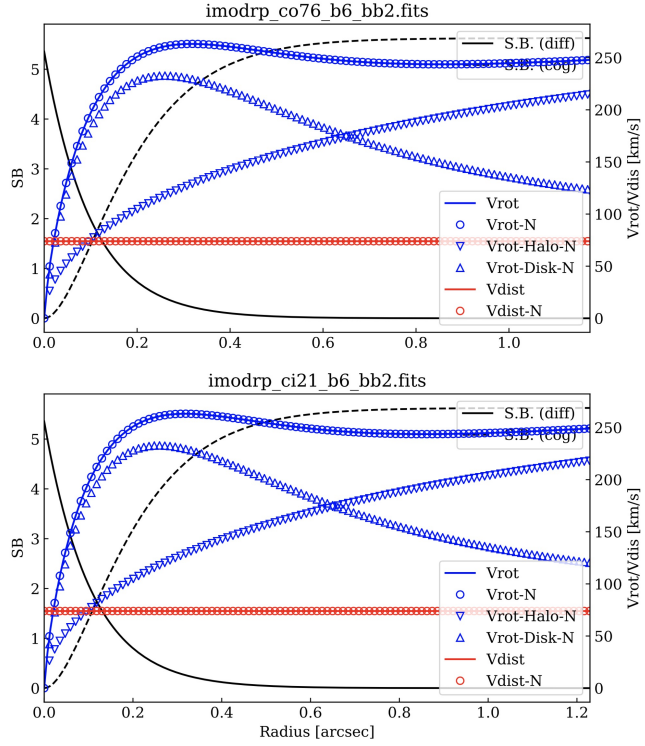


Figure 6. 1D diagnostic plots. Intensity vs. spatial: SB radial profile (after deprojection), Highlight the advantage of searching for high spatial frequency information in UV.

van Albada, T. S., Bahcall, J. N., Begeman, K., & Sancisi, R. 1985, ApJ, 295, 305, doi: [10.1086/163375](https://doi.org/10.1086/163375)

van der Hulst, J. M., Terlouw, J. P., Begeman, K. G., Zwitser, W., & Roelfsema, P. R. 1992, in Astronomical Society of the Pacific Conference Series, Vol. 25, Astronomical Data Analysis Software and Systems I, ed. D. M. Worrall, C. Biemesderfer, & J. Barnes, 131. <http://adsabs.harvard.edu/abs/1992ASPC...25..131V>

van der Kruit, P. C. 1988, A&A, 192, 117

van der Kruit, P. C., & Searle, L. 1981, A&A, 95, 105

van Diepen, G. N. J. 2015, Astronomy and Computing, 12, 174, doi: [10.1016/j.ascom.2015.06.002](https://doi.org/10.1016/j.ascom.2015.06.002)

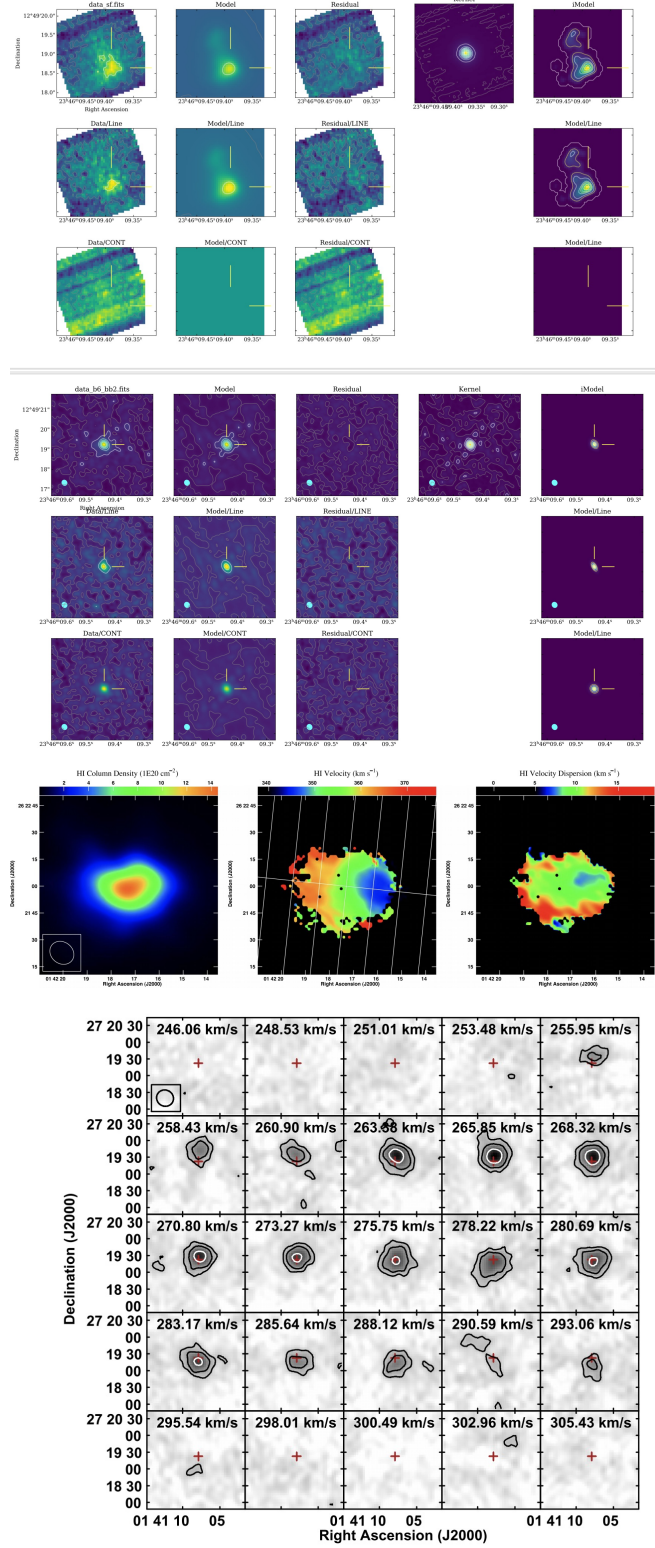


Figure 7. Highlight the advantage of searching for high spatial frequency information in UV.

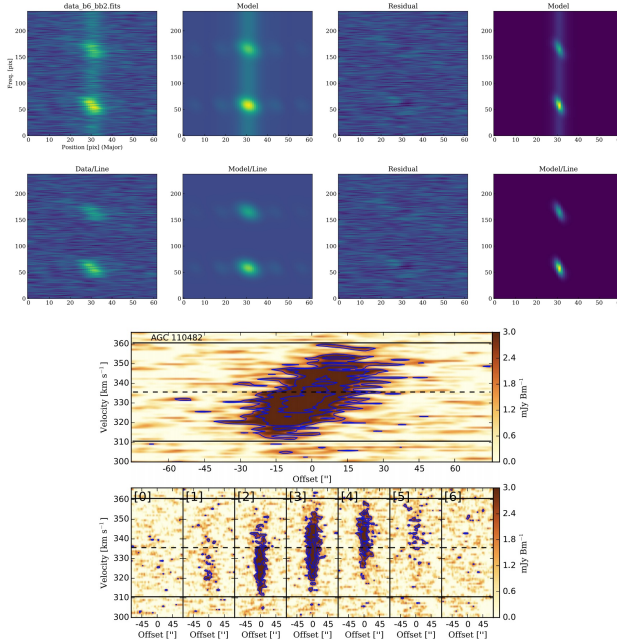


Figure 14. Spatially resolved P - V diagrams across the major and minor axes of AGC 110482. The upper panel shows the slice taken across what was identified as the “major axis” of rotation (see Table 2) and which passes through the kinematic center. The lower panels show minor axis P - V cuts, spaced evenly by one beam width along the major axis; the central panel intersects the major axis slice at the dynamical center position. The slices used to generate these P - V -maps are overlaid on the upper middle panel of Figure 1.

Figure 8. 1D diagnostic plots. Intensity vs. spatial: SB radial profile (after deprojection), Highlight the advantage of searching for high spatial frequency information in UV.